FULL PAPER

Ferroelectrics

**ADVANCED
FUNCTIONAL
MATERIALS**

www.afm-journal.de

A Coherently Strained Monoclinic [111]PbTiO₃ Film Exhibiting Zero Poisson's Ratio State

Yunlong Tang, Yinlian Zhu, Xiuliang Ma,* Zijian Hong, Yujia Wang, Wenyuan Wang, Yaobin Xu, Ying Liu, Bo Wu, Lang Chen, Chuanwei Huang, Longqing Chen, Zuhuang Chen, Haijun Wu, and Stephen J. Pennycook*

[111]-Oriented perovskite oxide films exhibit unique interfacial and symmetry breaking effects, which are promising for novel quantum materials as topological insulators and polar metals. However, due to strong polar mismatch and complex structural reconstructions on (111) surfaces/interfaces, it is still challenging to grow high quality [111] perovskite heterostructures, let alone explore the as-resultant physical properties. Here, the fabrication of ultrathin $PbTiO_3$ films grown on a $SrTiO_3$(111) substrate with atomically defined surfaces, by pulsed laser deposition, is reported. High-resolution scanning transmission electron microscopy and X-ray diffraction reveal that the as-grown [111]$PbTiO_3$ films are coherent with the substrate and compressively strained along all in-plane directions. In contrast, the out-of-plane lattices are almost unchanged compared with that of bulk $PbTiO_3$, resulting in a 4% contraction in unit cell volume and a nearly zero Poisson's ratio. Ferroelectric displacement mapping reveals a monoclinic distortion within the compressed [111]$PbTiO_3$, with a polarization larger than 50 μC cm⁻². The present findings, as further corroborated by phase field simulations and first principle calculations, differ significantly from the common [001]-oriented films. Fabricating oxide films through [111] epitaxy may facilitate the formation of new phase components and exploration of novel physical properties for future electronic nanodevices.

1. Introduction

For functional perovskite oxides materials, [001]-oriented epitaxy is mature that the manipulations of phase transitions and performances of perovskite materials were largely facilitated.[1–10] However, the strain states of a [001] epitaxy display extremely high symmetry, which is insufficient for novel manipulations of interfacial effects and phase components involving deep symmetry breaking effects. Other than [001] epitaxy, several theoretical works have shown that high-index axis epitaxy, such as [111]-oriented epitaxy, offers novel opportunities for introducing new interfacial effects, strain states, and symmetry breaking effects into perovskite oxide films.[11–16] For example, different types of new monoclinic ferroelectric phases were identified in [111]$PbTiO_3$, [111]$BaTiO_3$, and [111]$PbZr_{1-x}Ti_xO_3$ films by mean-field thermodynamic, density-functional theory calculations, and phenomenological Ginzburg–Landau–Devonshire thermodynamic model.[11–14] Importantly, novel responses such as strain-induced diffuse dielectric

Dr. Y. Tang, Prof. Y. Zhu, Prof. X. Ma, Dr. Y. Wang, Dr. W. Wang,
Dr. Y. Xu, Dr. Y. Liu, B. Wu
Shenyang National Laboratory for Materials Science
Institute of Metal Research
Chinese Academy of Sciences
Wenhua Road 72, 110016 Shenyang, China
E-mail: xlma@imr.ac.cn
Prof. X. Ma
State Key Lab of Advanced Processing and Recycling
on Non-ferrous Metals
Lanzhou University of Technology
Langongping Road 287, 730050 Lanzhou, China
Dr. Z. Hong, Prof. L. Chen
Department of Materials Science and Engineering
The Pennsylvania State University
University Park
PA 16802, USA

Prof. L. Chen
Department of Physics
South University of Science and Technology of China
518055 Shenzhen, China
Dr. C. Huang
School of Materials Science and Engineering
Shenzhen University
518060 Shenzhen, China
Dr. Z. Chen
School of Materials Science and Engineering
Harbin Institute of Technology
Shenzhen, Guangdong 518055, China
Dr. H. Wu, Prof. S. J. Pennycook
Department of Materials Science and Engineering
National University of Singapore
Singapore 117576, Singapore
E-mail: steve.pennycook@nus.edu.sg

**ADVANCED
SCIENCE NEWS**
www.advancedsciencenews.com

**ADVANCED
FUNCTIONAL
MATERIALS**
www.afm-journal.de

anomaly and critical point effect were further predicted in [111]$PbTiO_3$ films.[11] Moreover, unusual ferroelectric polarization reversal through successive ferroelastic transitions was confirmed in [111] $PbZr_{0.2}Ti_{0.8}O_3$ films, which is distinct from common [001] ferroelectric films.[16] In addition, some [111] perovskite films were predicted to display topological insulating effect by tight-binding modeling and first-principles calculations, such as [111]$LaAuO_3$ bilayers.[15] Furthermore, polar metal was accomplished recently in [111]$NdNiO_3$ films by the geometric constrain from $LaAlO_3$(111) substrates,[17] which is extremely rare in nature since free carriers can naturally eliminate possible internal dipoles within a metal.

Nevertheless, unlike the well-studied [001]-oriented perovskite epitaxial films, several challenges remain here for accessing a high quality [111]-oriented perovskite oxide film. First, the (111) surfaces of perovskite oxides are highly charged and unstable.[18–21] Moreover, (111) perovskite oxide interfaces are generally under a highly polar mismatch state.[18–21] For instance, the (001) surfaces/interfaces of many perovskites are nominally neutral, while their (111) surfaces are highly charged. Specifically, $PbTiO_3$ consists of alternating $Pb^{2+}O^{2-}$ and $Ti^{4+}O_2^{2-}$ along [001], which are both nominally neutral layers. When viewed along [111] direction, $PbTiO_3$ consists of alternating $Pb^{2+}O_3^{2-}$ and Ti^{4+}, which contains planes of charge ± 4 per unit cell. These charges further induce large polar mismatches between different (111) layers. Thus unavoidable reconstructions could easily occur and unexpected phases may thus evolve during the [111] film growth.

In this study, by fine control of the growth condition, we report the successful preparation of high quality $PbTiO_3$ ultrathin films on $SrTiO_3$(111) substrates. We find that the symmetry of the substrate is allowed to deliver to the $PbTiO_3$ films, which leads to exotic properties as monoclinic, highly polar $PbTiO_3$ phase exhibiting zero Poisson's ratio state. These monoclinic [111]$PbTiO_3$ films are coherent and compressively strained along all in-plane directions, while the out-of-plane lattice was found almost unchanged compared with bulk $PbTiO_3$, resulting in 4% contraction in unit cell volume and a nearly zero Poisson's ratio, as revealed by aberration-corrected scanning transmission electron microscope under high angle annular dark field mode (HAADF-STEM) and X-ray diffraction (XRD). These results were further confirmed by phase field simulations and first principle calculations. This work demonstrates that [111] epitaxy is a new way to mediate novel phase components and properties of perovskite oxides.

2. Results and Discussion

We grew ultrathin epitaxial $PbTiO_3$ films by pulsed laser deposition (PLD), which are constrained by a $SrTiO_3$(111) substrate (see more details in the Supporting Information). By optimizing the growth rate via tuning laser energy and frequency, [111]$PbTiO_3$ films strained (coherent) along all in-plane directions were obtained. The symmetry of the substrate is imposed on the $PbTiO_3$ films, leading to exotic properties, specifically, large 3D compressed unit cell volume with extreme Poisson's ratio (PR), which is nearly zero at room temperature. Moreover, the $SrTiO_3$(111) surface exhibits a threefold rotational symmetry about the surface normal, which

has further promoted polarization along the cube diagonal (P_R) in the compressed [111]$PbTiO_3$ films. Thus, the original polarization of the tetragonal $PbTiO_3$ phase (P_T) has been severely rotated, giving rise to a low symmetry phase with monoclinic distortion (P_M). The obtained monoclinic phase in [111]$PbTiO_3$ films is highly polar with clear piezoelectric response, and shows a ≈4% volume contraction in response to the nearly zero PR value, as evidenced by aberration-corrected HAADF-STEM and XRD (detailed in the Supporting Information).

Bulk $PbTiO_3$ (PTO) is tetragonal with lattice parameters of $a = b = 3.904(0)$ Å and $c = 4.157(5)$ Å.[22] $SrTiO_3$ (STO) is cubic with lattice parameters of $a = 3.905$ Å.[2] The unit-cell volumes of PTO (V_{PTO}) and STO (V_{STO}) are 63.365 and 59.547 Å^3, respectively. Thus the nominal average lattice parameter of PTO can be estimated as $\sqrt[3]{V_{PTO}}$, which is $a_n = 3.987$ Å and would induce a nominal compressive strain $-(a_n/a_{STO} - 1)$ of ≈2.1% on the PTO film when it is coherent.

PTO films with thicknesses of 6 and 15 nm, respectively, were grown on STO(111) substrates. We find that the film surfaces are extremely flat with negligible roughness (**Figure 1**A–D; Figures S1 and S2, Supporting Information). High magnification images of the coherent interfaces are shown in Figure 1E,F. Atomic force microscopy (AFM) morphology mapping further confirms the flat PTO(111) surface with a RMS roughness less than 0.2 nm over an area of 3×3 μm^2 (**Figure 2**A). (111) XRD peaks for both films are shown in Figure 2B (detailed in the Supporting Information). Obvious thickness fringes further indicate the smoothness of the surface and the high quality of the 15 nm [111]PTO film.

If the film is fully relaxed, the spacing of misfit dislocations is estimated to be approximately 16 nm based on the nominal mismatch value of 2.1%.[23] However, the present PTO/STO interfaces are completely coherent, which means that the [111]PTO films are fully strained (Figure 1A,B; Figure S2, Supporting Information).

We extract strains from HAADF-STEM images using 2D Gaussian fitting of atomic positions[24–32] (Supporting Information). By using the STO as a reference, we measure the in-plane and out-of-plane strains from both ⟨110⟩ (6 nm [111]PTO film) and ⟨112⟩ (15 nm [111]PTO film) projections, as shown in **Figure 3**A,B, respectively. Both measurements show similar strain distributions which indicate that the unique strain states in the 6 and 15 nm films are the same and independent of projected orientations.

The in-plane lattice parameters of the 6 and 15 nm [111]PTO films are nearly constant, confirming the films are indeed not relaxed by defects. The out-of-plane strains in the [111]PTO films are ≈2% enlarged along the [111] direction. It should be emphasized that although the out-of-plane (111) spacings of these films are enlarged compared with that of the STO substrate, they are almost unchanged when compared with bulk tetragonal PTO lattice (≈2.3 Å; the (111) planar spacing for STO is 2.255 Å). Thus these [111]PTO films are actually compressed in 3D, which is completely different from compressively strained [001]$PbZr_{0.2}Ti_{0.8}O_3$ films.[33,34] X-ray diffraction further corroborates that the PTO(111) planar spacings are about 2.3 Å (Figure 2B). Since the (111) plane of STO and PTO share the same area (same in-plane strain, Figure 3A,B) and only the [111] direction of PTO is elongated, the unit cell volume of PTO
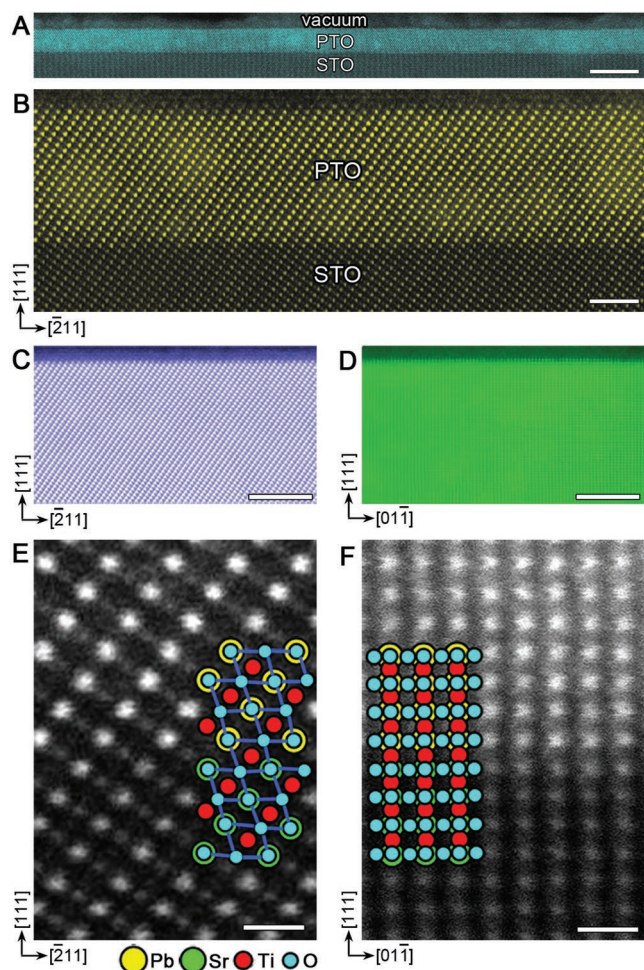
Figure 1. HAADF-STEM images of [111]PbTiO₃ films on SrTiO₃(111). A) Low- and B) high-magnification images of a 6 nm film viewed along ⟨110⟩ SrTiO₃. C,D) Surface structures, and E,F) magnified interface structures of a 15 nm film viewed along ⟨110⟩ and ⟨112⟩, respectively. The atomic structures are shown as two insets in (E) and (F), where the yellow circles correspond to Pb^{2+} columns (superposed with O^{2-} anions, small blue circles); green and red circles denote Sr^{2+} (superposed with O^{2-}) and Ti^{4+} columns, respectively. Pure O^{2-} columns contribute negligible image intensity due to their small Z. Scale bars: A), 10 nm; B), 2 nm; C,D), 5 nm; E) and F), 0.5 nm.

compared with STO should also expand by 2%. This results in $V_{PTO} = V_{STO} \times (1.02) = 59.547$ Å³ $\times (1.02) = 60.738$ Å³. Compared with its bulk value of 63.365 Å³, the unit cell volumes of our [111]PTO films shrink by ≈4%. Such a volume contraction is comparable to that obtained in the PTO powder samples under hydrostatic pressure of about 5 GPa.[35,36] The unit-cell volume distribution of the 15 nm film is shown in Figure 3C, which is calculated via the out-of-plane lattice distribution (Figure 3B). Out-of-plane strain peaks for PTO(111) planes near the PTO/STO interfaces were observed (Figure 3A,B), which may originate from interfacial defects like oxygen vacancies. We note that these defects contributing to lattice expansion in perovskite oxide were also observed in previous work at PbTiO₃/BiFeO₃ interfaces.[37]

To further demonstrate this unusual strain state in our [111] PTO films, a 6 nm [001]-oriented PTO film on STO(001) substrate is used as a reference (**Figure 4**; Figure S3, Supporting Information), which was grown simultaneously with the 6 nm [111]PTO film. It is seen that the out-of-plane strain (c lattice) here shows obvious lattice compression in response to possible screening of ferroelectricity induced charges near the interface and surface (Figure 4B). The bulk PTO c lattice (4.157 Å here) can be extracted from the central five unit cells. Thus the PTO unit cell volume is estimated as 63.390 Å³, which is consistent with previous results.[22] The comparisons between these simultaneously grown [111] and [001]PTO films here corroborate the intrinsic and unusual strain states of the present [111]PTO films, which are caused by the high index constraints from the STO(111) substrates. The unique (111) strain of these [111]PTO films is further corroborated by high-resolution TEM imaging (Figure S4, Supporting Information).

The unit cell volume contraction relative to the [001]PTO film (63.390 Å³) is shown in Figure 3C, where more than 4% volume contraction is extracted. This result is distinct with previous reports for PbZr₀.₂Ti₀.₈O₃ films grown on STO(001), where the compressed PbZr₀.₂Ti₀.₈O₃ ($a = b = 3.953$ Å, $c = 4.148$ Å) tend to retain their unit cell volumes (slightly expanded by 0.5% in ref. [33] and slightly shrunk by 0.7% in ref. [34]). By only taking the lattice spacings into account, we propose that such distortions may induce $R3m$-like (rhombohedral symmetry) phase the present PTO films. Our observations support recent predictions that [111]PTO films exhibit $R3m$ structure under compression.[11,12,14]
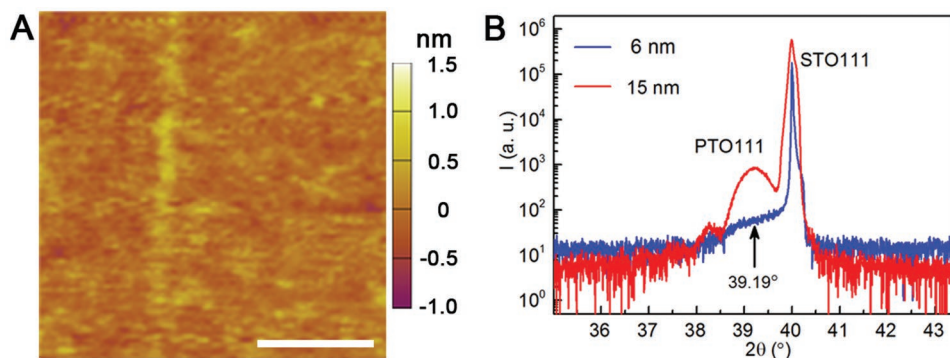

Figure 2. Surface morphology and X-ray diffraction analysis. A) An AFM image showing the surface morphology of the as-received 6 nm [111]PbTiO₃ film. Scale bar: 1 μm. B) X-ray diffraction results showing the pseudocubic 111 peaks of the films (arrowed).
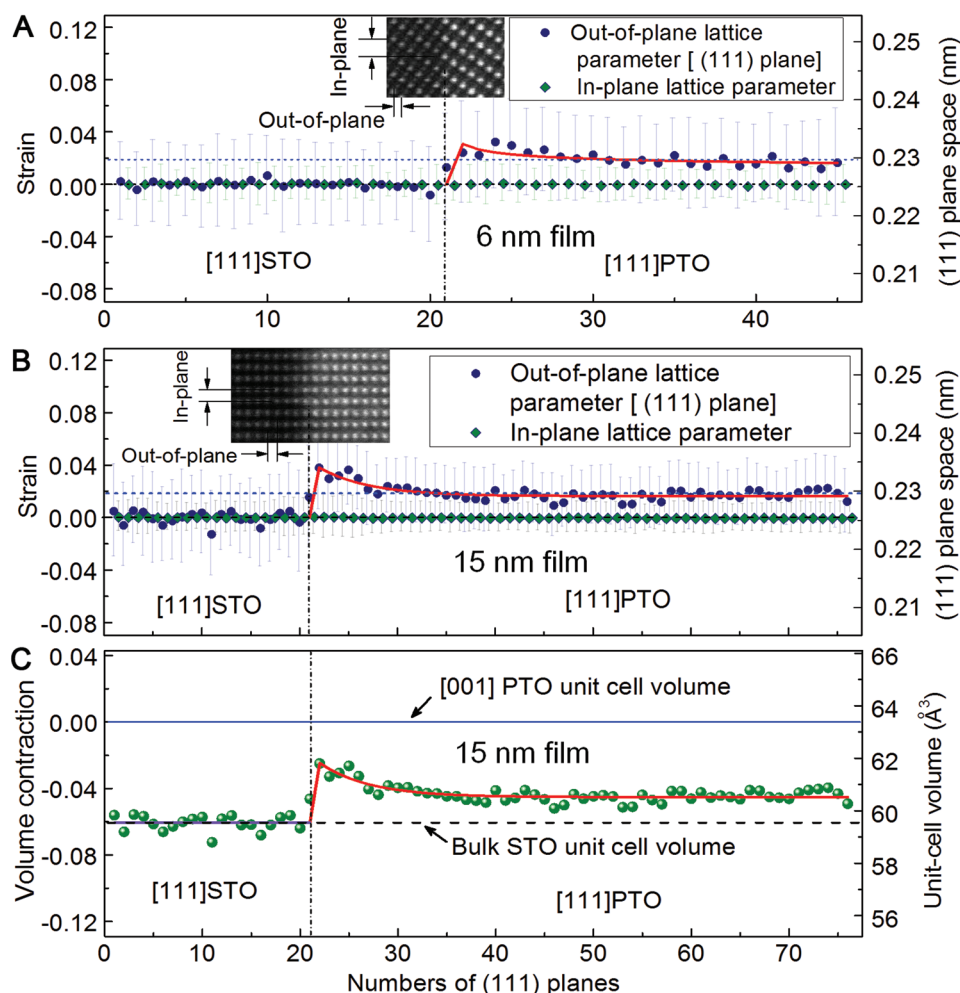
Figure 3. Lattice parameter analysis for the [111]PbTiO₃ films. A, B) In-plane and out-of-plane lattice parameter distributions of the 6 and 15 nm films, respectively. Horizontal blue dashed lines mark the (111) spacing of the bulk tetragonal PbTiO₃ (about 0.230 nm). C) Unit-cell volume distribution of the 15 nm film along the out-of-plane direction. Note the large 3D unit cell volume contraction.

Thus we can estimate the elastic behavior of these [111]PTO films. Since the (111) planes of the present PTO films were unchanged compared with bulk PTO, the PR of this strain state can be estimated as nearly zero. This is also the reason that the unit cell volumes of these [111]PTO films were compressed by more than 4%. How the atomic structures and other properties like ferroelectric and piezoelectric responses should react with this extreme PR value are thus intriguing topics needing further exploring.

We have further performed reciprocal space map (RSM) analysis to illustrate the strain state of the 15 nm [111]PTO film on a much larger scale. **Figure 5**A,B,C is RSMs recorded around the STO 111, 132, and 312 Bragg peaks. The PTO 111 peak (Figure 5A) is consistent with the line scan shown in Figure 2B, which confirms that the (111) spacing of the [111] PTO film is ≈2.3 Å. Moreover, both the PTO 132 and 312 peaks exhibit undetectable in-plane shifts from the corresponding STO 132 and 312 peaks, which imply that the [111]PTO film is indeed not relaxed. All above HAADF-STEM, AFM, and XRD results thus consistently reveal that coherent [111]PTO films displaying unique 3D volume contraction were obtained.

We have studied the atomic structures of these [111]PTO films more deeply. We have observed clear monoclinic shear strain in these [111]PTO films (**Figure 6**, the fast scan direction of the HAADF-STEM imaging was adjusted to be parallel with the out-of-plane [111] direction, so that the effect of scan noise is minimized). The (11$\bar{2}$) planes of the [111]PTO films shear gradually toward the [11$\bar{2}$] direction, which can be extracted via geometric phase analysis[9,38,39] (GPA). This low symmetry shear strain unequivocally indicates that the symmetry of the [111]PTO films was further lowered and cannot be described as R3m. Both the 6 nm (blue curve) and 15 nm [111]PTO (red curve) films show obvious monoclinic shear strains. The shear strains for the 15 nm film saturates at ≈4%, which corresponds to a shear angle of ≈2.3° (shear strain ≈ 0.04 ≈ tan (2.3°)).

We further studied the atomic scale polar behaviors of these [111]PTO films, which are of high importance for understanding the polarization and piezoelectric behaviors of PTO. Although it is hard to directly measure the polarization in such thin ferroelectrics due to problems like leakage,[26,40] we successfully estimate the polar behavior of the present [111] PTO films through the identification of local dipoles formed by
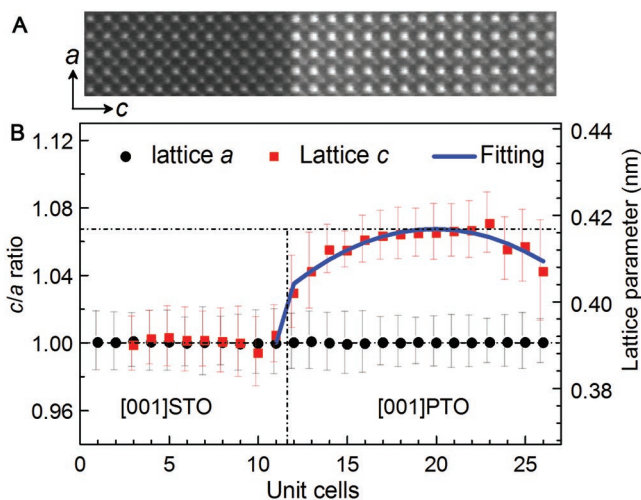
Figure 4. Atomic imaging and lattice parameter analysis for a 6 nm [001] PbTiO₃ film. A) An atomic resolved HAADF-STEM image of the 6 nm [001]PbTiO₃ film viewed along [010]SrTiO₃, grown simultaneously with the 6 nm [111]PbTiO₃ film. B) In-plane and out-of-plane lattice parameter distributions of the [001]PbTiO₃. These parameters were extracted directly from the raw HAADF-STEM image. Horizontal black dashed lines mark the c/a ratio or c lattice spacing of the bulk tetragonal PbTiO₃ (about 1.065 or 0.4157 nm).

charge separation between negatively charged O^{2-} octahedra and positively charged cations. For this purpose, the O^{2-} columns as well as the cations should be recorded simultaneously. Thus bright-field-STEM (BF-STEM) imaging was performed[41] (Supporting Information).

Figure 7A shows an atomic resolution BF-STEM image of the 6 nm [111]PTO film, where O^{2-} columns are well distinguished. Contrast is inverted here to ease visual inspection. A representative area marked by a red box is magnified and shown as an inset. The charge separation manifests as relative displacements of the O^{2-} octahedra to Ti^{4+} (δ_{Ti-O}), as indicated by the atomic schematics in Figure 7A, forming electric dipoles in the PTO unit cells. The paraelectric, nonpolar essence of STO can be seen in Figure 7A, since there is no identifiable δ_{Ti-O} throughout the STO substrate. In particular, clear ferroelectric switching behavior and potential piezoresponse of the 15 nm [111]PTO film were observed in local piezoresponse force microscopic (PFM) measurement, as seen in the well-defined phase hysteresis loops (Figure 7B) and amplitude signals (Figure 7C). The relationship between spontaneous polarization P_s and off-center displacement of ions is[42,43]

$$P_s = 1/V \sum Z_i \Delta_i \tag{1}$$

where V, Z_i, and Δ_i are the volume of the unit cell, the effective charge, and the off-center displacement of ion i, respectively. In particular, according to the linear relation between polarization and atom displacement in displacive ferroelectrics,[44] the P_s can be estimated by the following expression

$$P_s = k\delta_{Ti-O} \tag{2}$$

where the constant $k = 2726$ ($\mu C\ cm^{-2}$) nm^{-1}.[34,45] Previously, this simplified estimation (2) based on δ_{Ti-O} and Equation (1) was successfully used to evaluate polarization in tetragonal $PbZr_{0.2}Ti_{0.8}O_3$ films.[26,34] The δ_{Ti-O} is calculated as a vector between each Ti^{4+} and the center of mass of its two nearest neighbors O^{2-} (Supporting Information). We extract a 2D δ_{Ti-O} vector map based on the BF-STEM image, as shown in Figure 7D. The magnitude of the δ_{Ti-O} distribution across the 6 nm [111]PTO film is given in Figure 7E. The δ_{Ti-O} is compressed near the surface and interface, which is due to the possible compensation of the polar interfaces. According to this statistical result, the δ_{Ti-O} is about 0.18 Å in the center of the film, which corresponds to an ≈50 $\mu C\ cm^{-2}$ spontaneous polarization. It is worthwhile to note that a possible P_s component along the viewing direction was not identified here, thus the full P_s of the present [111]PTO films is probably larger than 50 $\mu C\ cm^{-2}$. Considering the monoclinic distortion observed here (Figure 6), these observations indicate that the polarization distributions (not along the [111] direction) in the present PTO films are rotated neither along [111] nor ⟨001⟩. So the interaction of the extreme PR and tetragonal PTO bulk unit cells must have already lowered the symmetry further to monoclinic space groups such as *Cm* (M_A or M_B) or *Pm* (M_C) or O groups, where the polar axis rotates in the pseudocubic {110} planes or {100} planes, respectively.

To gain further insight into the atomic scale lattice, polarization and phase behaviors of these uniquely strained [111] PTO films, we have performed anisotropic elasticity theory, first-principles and phase field based theoretical calculations. Details of these theoretical simulations are given in Supporting Information and Figures S5–S7 in the Supporting Information.[10,12,13,42,46–51] First our anisotropic elastic calculations have confirmed that the extreme PRs including negative and zero values could arise in tetragonal PTO due to elastic anisotropy (Figure S5, Supporting Information).
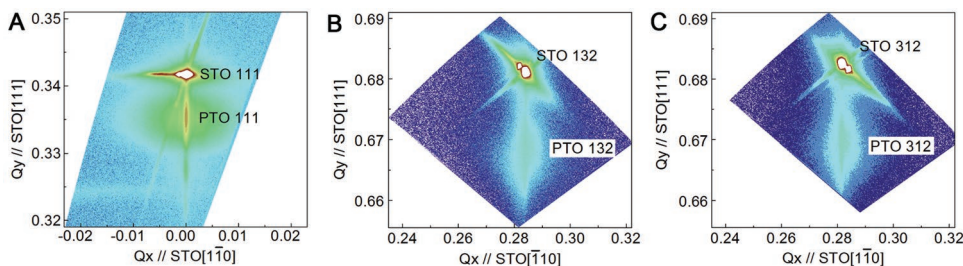

Figure 5. Reciprocal space map (RSM) analysis for the 15 nm [111]PbTiO₃ film. A,B,C) RSMs recorded around the STO 111, 132, and 312 Bragg peaks.

ADVANCED
SCIENCE NEWS
www.advancedsciencenews.com

ADVANCED
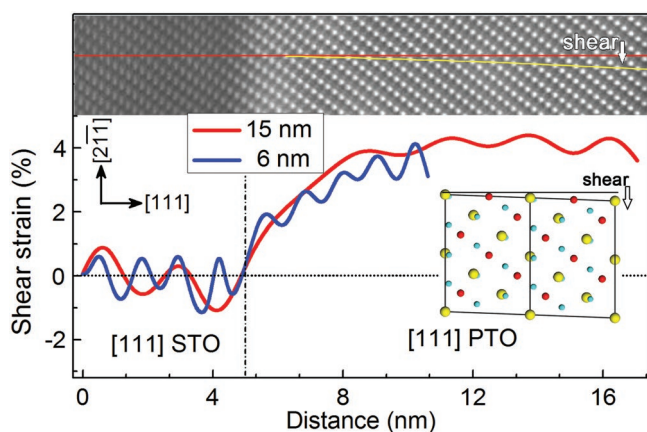**FUNCTIONAL**
MATERIALS
www.afm-journal.de

Figure 6. Monoclinic shear strain extracted via geometric phase analysis (GPA). The inset in the upper panel is a HAADF-STEM image of the 15 nm [111]PbTiO$_3$ film. One can see that while the (11$\bar{2}$) planes of the SrTiO$_3$(111) substrate aligns persistently along the horizontal direction (red line), the (11$\bar{2}$) planes of the [111]PbTiO$_3$ films (yellow line) shear gradually toward the [11$\bar{2}$] direction. The inset in the lower right panel depicts the atomic structure of the monoclinic [111]PbTiO$_3$.
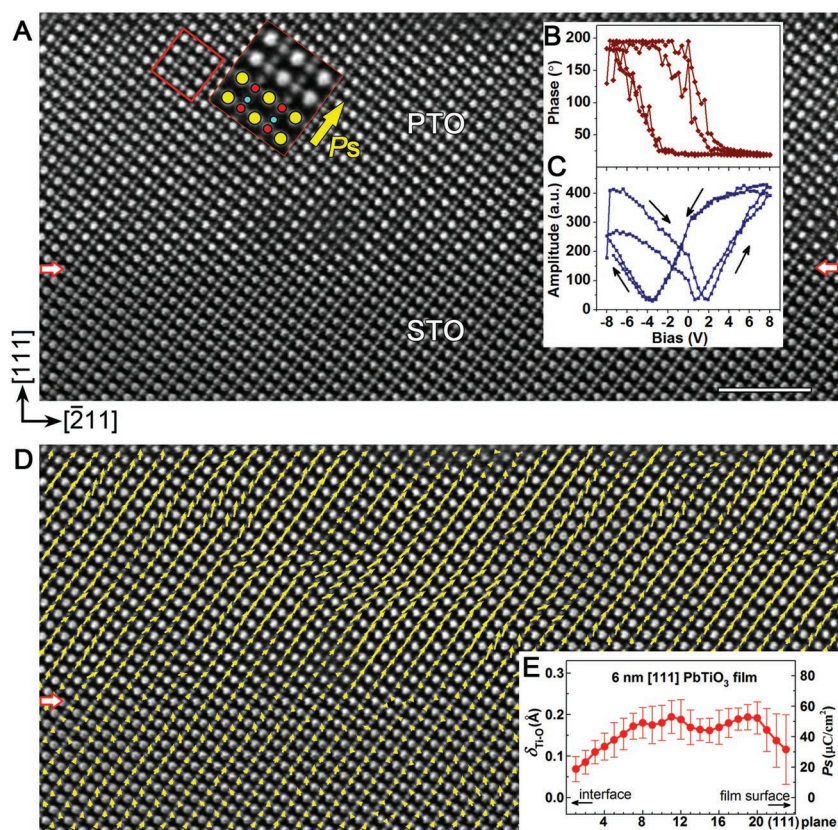
Figure 7. Experimental evidence for the low symmetry polar PbTiO$_3$ phase grown on SrTiO$_3$(111). A) BF-STEM image of the 6 nm [111]PbTiO$_3$ film showing O^{2-} columns. Scale bar: 2 nm. Contrast is inverted here to ease visual inspection. The red box area is magnified as an inset, which displays the significant Ti–O (δ_{Ti-O}) displacement. Local PFM hysteresis loops are shown in phase B) and amplitude signals C), respectively. D) The δ_{Ti-O} displacement vector maps based on A). E) The statistical distribution of the δ_{Ti-O} displacement inside the [111]PbTiO$_3$ film.

Figure 8A,B shows first-principles relaxation results of [111] PTO under the constraint of a STO(111) substrate, along [0$\bar{1}$1] and [$\bar{2}$11] projections, respectively. The upper parts of these two images depict the ideal cubic, nonpolar structure for comparison. Note the obvious O displacements from the centrosymmetric location in the polar [111]PTO lattice (Figure 8A,B, marked by two pairs of black arrows) and the accompanying relative shift of O octahedra (Figure 8A, marked by a dashed diamond), which is consistent with the BF-STEM results (Figure 7A,D). Particularly, in the polar [111]PTO the O shifts neither along [011] nor along [111], as indicated by the black arrow pairs in Figure 8A, suggesting a low symmetry polar PTO phase. The final P_s direction from the first-principles relaxation lies in a (110) type crystal plane (as marked in Figure 8B), whose magnitude is about 67 µC cm^{-2}. The polarization rotation angle (θ) is about 25.7° and the original tetragonal c axis also inclines by about 1.2° in the (110) plane correspondingly. As a result, the [111]PTO actually possesses a monoclinic Cm (M$_A$) space group. This angle is somewhat smaller than the experimental values ($\approx$2.3°), which may be the result of the underestimated c/a ratio from first-principle calculations (the theoretical value 1.043, while the experimental one is 1.065). We note that the previous first-principle result indicated that there are two types of monoclinic Cm PTO phases when strained by (111) substrates, M$_A$ and M$_B$.[12] We have further considered both models for the PTO/STO(111) system and found their energies are very close, which means both phases may coexist in the present [111]PTO films. We also note that highly polar, monoclinic [111]PTO films are consistent with recent first-principles calculations on the PTO/STO(111) system.[47,48]

Here in our first-principles calculation, the in-plane compression for [111]PTO is about −2.3% and the out-of-plane (111) spacing increases by $\approx$1%. As a result, the unit cell volume of the [111]PTO film reduces by $\approx$2%, which is smaller than the experimental one ($\approx$4%). One main reason is that the LDA function underestimates the lattice parameters of tetragonal PTO. Another possible reason is that the depolarization field (not considered in the first-principles calculation) should further reduce the out-of-plane polarization and lattice parameter.

We perform phase-field simulations to further unveil the polar structure of the [111]PTO films on STO(111) substrate (Figures S6, and S7 and Table S1, Supporting Information). It was demonstrated that a highly polar, low symmetry monoclinic phase was formed, which agrees well with our experimental observations and first principles calculations. The strain states and polarization distribution of this film are plotted in Figure 8C. Consistent with the experimental measurement, an out-of-plane strain of $\approx$2% is observed (the reference state is the (111)
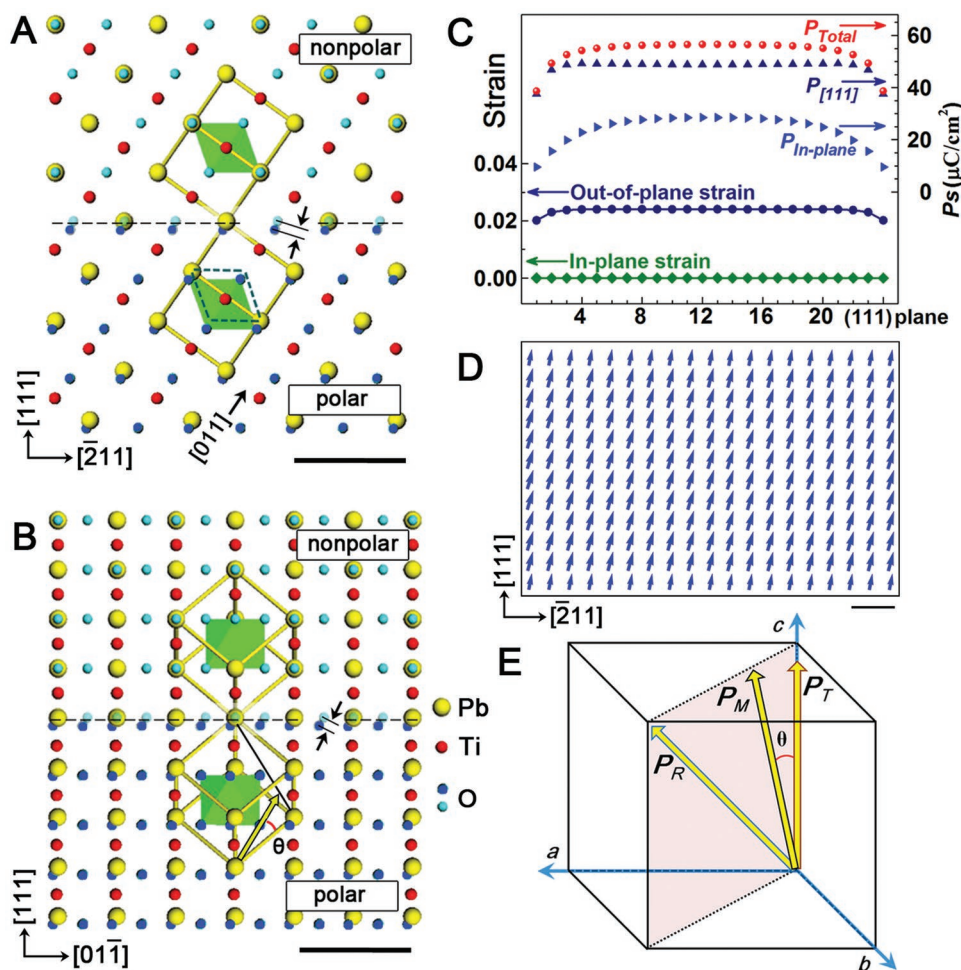
Figure 8. Theoretical evidence for the low symmetry polar phase PbTiO$_3$ showing zero Poisson's ratio. A, B) Schematic diagrams showing the first-principles relaxation results of [111]PbTiO$_3$ strained on a SrTiO$_3$(111) substrate, viewed along [0$\bar{1}$1] and [$\bar{2}$11]. Scale bars: 0.5 nm. Yellow circles: Pb; red circles: Ti; blue and light blue circles: O atoms in polar and nonpolar PTO lattices, respectively. Polarization rotation angle (θ) away from the cubic axis is marked in B), which swings within the {110} plane. C) Phase field simulation results of strain and polarization distributions for a 6 nm [111] PbTiO$_3$ film. Note the strain behavior here is consistent with the experimentally observed one. D) A polarization vector map of the 6 nm [111]PbTiO$_3$ film viewed along [0$\bar{1}$1]. Scale bar: 1 nm. Note that possible polarization projection along the viewing direction may exist depending on the specific monoclinic distortion directions. E) A schematic illustration demonstrating the polarization rotation within the {110} plane.

planar spacing of the STO substrate), while the in-plane direction is fully strained, indicating also a nearly zero PR value. The total polarization from our phase-field simulation is about 60 µC cm^{-2}, which is consistent with the experimental value. This value is slightly smaller than the polarization of bulk PTO. The monoclinic polarization rotation angle relative to the original tetragonal c axes here is ≈18° to 24°. A polar vector projection mapping is further given in Figure 8D. Figure 8E shows the polarization rotation schematic within the {110} planes.

Our results demonstrate that high quality [111]PbTiO$_3$ films with atomically defined flat surface can be obtained. Moreover, novel phase components and unique response could be further achieved through [111] epitaxy. There are two types of crystallographic axes on the (111) surfaces of perovskite crystals (Figure S8, Supporting Information), namely ⟨112⟩ and ⟨110⟩. Both are high index axes compared to the principle ⟨100⟩ type crystallographic axes. The zero Poisson's ratio observed here is consistent with recent theoretical studies that extreme Poisson's

ratios are actually common for materials ranging from metals to oxides and so on, especially when crystals were deformed along high-index axes,[52–54] although till recently it was thought that negative or zero Poisson's ratio were rare in nature.[52,55]

The large 3D volume contraction resulting from the nearly zero Poisson's ratio is stabilized by a unique monoclinic PbTiO$_3$ phase which was never seen before in common temperature-structure phase diagrams of PbTiO$_3$.[44] The Pb–O hybridization, which is strongly related to the negative thermal expansion of tetragonal PbTiO$_3$, is probably also contributing to the large volume contraction here.[49,50] The monoclinic PbTiO$_3$ exhibits a high polarization value which is almost comparable to the original bulk PbTiO$_3$. Moreover, clear polarization rotation and piezoelectric signals were observed for these novel monoclinic [111]PbTiO$_3$ films. These findings imply novel methods for tuning polar behavior in ferroelectric oxides. Particularly, polarization rotations and monoclinic phases are known to be of great importance for piezoelectric responses of

**ADVANCED
SCIENCE NEWS**

www.advancedsciencenews.com

**ADVANCED
FUNCTIONAL
MATERIALS**

www.afm-journal.de

complex perovskite ferroelectrics,[35,56–62] as some recent works directly confirmed by experiments that the monoclinic perovskite ferroelectrics exhibit intrinsically large lattice strains and piezoelectric responses.[56,57] Thus the present work gives further opportunities for achieving high performance piezoelectric properties in simple perovskite oxides without utilizing complex components.[35] Moreover, possible monoclinic domain structures may evolve in these strained [111]PbTiO$_3$ films. Nevertheless, large volume contraction observed here is not affected by potential domain variants.

It should be emphasized that in the present 2D films, the in-plane strains actually compress the [111]PbTiO$_3$ films in two directions. Thus the estimated zero Poisson's ratio here is actually not the one strictly defined as a consequence of a uniaxial load. However, by considering all these factors, one can deduce that the exact Poisson's ratios of tetragonal PbTiO$_3$ crystal when deformed uniaxially along ⟨112⟩ or ⟨110⟩ are actually negative values, since no out-of-plane expansion occurs here even the PbTiO$_3$ crystal was compressed simultaneously from both ⟨112⟩ and ⟨110⟩ in-plane directions. This inference is reasonable because recent theoretical and survey studies also clearly revealed that negative Poisson's ratios occur along high index axes for many single crystals including PbTiO$_3$.[52,53]

For possible applications, we note that when a crystal exhibits zero or negative Poisson's ratios compressed along a specific direction, it would also be compressed in the lateral directions (so-called auxetic behavior[54]) or remain undeformed. This counterintuitive property could have many important applications as novel functional devices such as force amplifiers, micromechanical manipulation elements, indentation or shear resistant materials, sound or shock absorption coatings, self-adaptive vibration damping materials, and medical artery dilators.[52–54] Thus we hope this work will facilitate future studies on novel designs of potential devices through [111] epitaxy.

3. Conclusion

In summary, applying a symmetry constraint through a high-index substrate surface, we have successfully grown fully coherent [111]PbTiO$_3$ films displaying an extreme elastic property, zero Poisson's ratio and highly polar monoclinic structures. This study provides a clear experimental prototype to explore the origin of such elastic anomalies and the resultant properties of perovskite oxides, via high-index 2D film growth. Future studies on engineering symmetry confinement on epitaxial films or superlattices could reveal further exotic physical behaviors and facilitate the development of novel nanoscale functional devices.

4. Experimental Section

Material Preparation: PbTiO$_3$ films were deposited by PLD, using a Lambda Physik LPX 305i KrF (λ = 248 nm) excimer laser. A sintered PbTiO$_3$ ceramic target (3 mol% Pb-enriched) was used. The target-substrate distance was 40 mm. The background pressure was 10^{-5} Pa.

During the growth of PbTiO$_3$ films, the substrate temperature was kept at 650 °C, with a laser energy density of ≈2.0 J cm^{-2}, a laser repetition rate of 1, 2, 4, 5, and 10 Hz, and an oxygen pressure of 20 Pa. 5 Hz of laser repetition frequency was identified for high quality [111]PTO film growth.

STEM Experiment and Strain Analysis: The samples for the STEM experiments were prepared by slicing, gluing, grinding, dimpling, and finally ion milling. A Gatan PIPS was used for the final ion milling. HAADF-STEM, BF-STEM images were recorded using an aberration-corrected scanning transmission electron microscope (Titan Cubed 60–300 kV microscope (FEI) fitted with a high-brightness field-emission gun (X-FEG) and double Cs corrector from CEOS, and a monochromator operating at 300 kV). The beam convergence angle was 25 mrad, and thus yielded a probe size of less than 0.10 nm under STEM mode.

All the lattice parameters and strains were measured along the fast scan direction so that scan noise was minimized. For determining the lattice strains and δ_{Ti-O} displacement vectors of the [111]PTO films, noise in the HAADF images was filtered by low-pass annular masks restricted to the instrument resolution limit of the image and the BF-STEM image was further filtered by Wiener filtering. The atom positions were determined accurately by fitting them as 2D Gaussian peaks using MATLAB. The δ_{Ti-O} was calculated as a vector between each Ti^{4+} and the center of mass of its two nearest neighbors O^{2-}. The directions of P_s vectors can thus be estimated by the δ_{Ti-O} vectors pointing from net negative to positive charges. The visualization of the 2D δ_{Ti-O} vectors was carried out using MATLAB.

XRD and AFM/PFM Measurements: A SmartLab X-ray diffractometer was used in the XRD measurement with a Cu target, which corresponds to a wavelength (λ) of 1.5406 Å (Cu Kα). The surface morphology and local ferroelectric properties were measured using an Asylum Research MPF-3D scanning probe microscope. Hysteresis loops were collected with a triangular pulse of 8.0 V in amplitude applied to the tip.

First-Principles Calculations: All the calculations were performed using the VASP code. The local density approximation (LDA) exchange-correlation functional was used with projector-augmented wave (PAW) method. The plane wave cutoff energy was chosen as 600 eV. The O 2s and 2p, Ti 3s, 3p, 3d, and 4s, and Pb 5d, 6s, and 6p electrons were treated as the valence electrons. The optimized lattice constants, a and c of PbTiO$_3$ were 3.867 and 4.033 Å, respectively.

A hexagonal cell was adopted to study the [111]PTO film[23]. The three axes were the [0$\bar{1}$1], [10$\bar{1}$], and [111] directions of the quasicubic unit cell. The in-plane lattice parameters, i.e., a, b, and γ, were fixed as those of STO and the out-of-plane lattice parameters, i.e., c, α, and, β were allowed to relax during the atomic relaxation. The polarization vectors of the supercells were calculated using the Berry phase method.

Phase Field Simulations: In this work, phase-field simulations were performed by solving the time dependent Ginzburg–Landau equations (TDGL) using the spontaneous polarization vector as the order parameter

$$\frac{\partial P_i}{\partial t} = -L\frac{\delta F}{\delta P_i} \quad (i = 1,3) \tag{3}$$

where t, L, and F are the evolution time, kinetic coefficients, and total free energy, respectively. The total free energy was calculated as the volume integral of each individual energy contributions, namely, the elastic, electric, Landau and gradient energies

$$F = \int (f_{elas} + f_{elec} + f_{Land} + f_{grad})dV \tag{4}$$

To model the (111)-oriented PTO thin film, we employ the coordinate transformation to transform all the vector and tensor components from the original Cartesian coordinate axes along the [100], [010], and [001] crystallographic directions to a new set of Cartesian coordinates along the [01$\bar{1}$], [2$\bar{1}\bar{1}$], and [111] crystallographic directions. The pseudocubic lattice constants for PTO and STO, which determine the in-plane misfit strain, were chosen to be 3.957 and 3.905 Å, respectively. The background

dielectric constant was set as 40. The short-circuit electric boundary condition was applied along the film surface and the film/substrate interface. The top surface of the film was assumed to be stress-free while the displacement in the substrate sufficiently far away from the film/substrate interface was zero. A 3D mesh of $40 \times 128 \times 48$ was employed with a grid spacing of 0.25 nm. Periodic boundary conditions were applied along the in-plane dimensions while a superposition method was implemented along the out-of-plane direction. The thicknesses of the substrate that allowed mechanical relaxation, film, and vacuum were 12, 24, and 12 grid points, respectively.

Supporting Information

Supporting Information is available from the Wiley Online Library or from the author.

Conflict of Interest

The authors declare no conflict of interest.

[1] D. G. Schlom, L.-Q. Chen, C.-B. Eom, K. M. Rabe, S. K. Streiffer, J.-M. Triscone, *Annu. Rev. Mater. Res.* **2007**, *37*, 589.

[2] D. G. Schlom, L.-Q. Chen, C. J. Fennie, V. Gopalan, D. A. Muller, X. Pan, R. Ramesh, R. Uecker, *MRS Bull.* **2014**, *39*, 118.

[3] J. H. Haeni, P. Irvin, W. Chang, R. Uecker, P. Reiche, Y. L. Li, S. Choudhury, W. Tian, M. E. Hawley, B. Craigo, A. K. Tagantsev, X. Q. Pan, S. K. Streiffer, L. Q. Chen, S. W. Kirchoefer, J. Levy & D. G. Schlom, *Nature* **2004**, *430*, 758.

[4] J. H. Lee, L. Fang, E. Vlahos, X. Ke, Y. W. Jung, L. F. Kourkoutis, J.-W. Kim, P. J. Ryan, T. Heeg, M. Roeckerath, V. Goian, M. Bernhagen, R. Uecker, P. C. Hammel, K. M. Rabe, S. Kamba, J. Schubert, J. W. Freeland, D. A. Muller, C. J. Fennie, P. Schiffer, V. Gopalan, E. Johnston-Halperin, D. G. Schlom, *Nature* **2010**, *466*, 954.

[5] K. J. Choi, K. J. Choi, M. Biegalski, Y. L. Li, A. Sharan, J. Schubert, R. Uecker, P. Reiche, Y. B. Chen, X. Q. Pan, V. Gopalan, L.-Q. Chen, D. G. Schlom, C. B. Eom, *Science* **2004**, *306*, 1005.

[6] R. J. Zeches, M. D. Rossell, J. X. Zhang, A. J. Hatt, Q. He, C.-H. Yang, A. Kumar, C. H. Wang, A. Melville, C. Adamo, G. Sheng, Y.-H. Chu, J. F. Ihlefeld, R. Erni, C. Ederer, V. Gopalan, L. Q. Chen, D. G. Schlom, N. A. Spaldin, L. W. Martin, R. Ramesh, *Science* **2009**, *326*, 977.

[7] G. Catalan, A. Lubk, A. H. G. Vlooswijk, E. Snoeck, C. Magen, A. Janssens, G. Rispens, G. Rijnders, D. H. A. Blank, B. Noheda, *Nat. Mater.* **2011**, *10*, 963.

[8] N. A. Pertsev, A. G. Zembilgotov, A. K. Tagantsev, *Phys. Rev. Lett.* **1998**, *80*, 1988.

[9] Y. L. Tang, Y. L. Zhu, X. L. Ma, A. Y. Borisevich, A. N. Morozovska, E. A. Eliseev, W. Y. Wang, Y. J. Wang, Y. B. Xu, Z. D. Zhang, S. J. Pennycook, *Science* **2015**, *348*, 547.

[10] Y. L. Li, S. Y. Hu, Z. K. Liu, L. Q. Chen, *Acta Mater.* **2002**, *50*, 395.

[11] A. K. Tagantsev, N. A. Pertsev, P. Muralt, N. Setter, *Phys. Rev. B* **2001**, *65*, 012104.

[12] R. Oja, K. Johnston, J. Frantti, R. M. Nieminen, *Phys. Rev. B* **2008**, *78*, 094102.

[13] A. Raeliarijaona, H. Fu, *J. Appl. Phys.* **2014**, *115*, 054105.

[14] R. Xu, J. Zhang, Z. Chen, L. W. Martin, *Phys. Rev. B* **2015**, *91*, 144106.

[15] D. Xiao, W. Zhu, Y. Ran, N. Nagaosa, S. Okamoto, *Nat. Commun.* **2011**, *2*, 596.

[16] R. Xu, S. Liu, I. Grinberg, J. Karthik, A. R. Damodaran, A. M. Rappe, L. W. Martin, *Nat. Mater.* **2015**, *14*, 79.

[17] T. H. Kim, D. Puggioni, Y. Yuan, L. Xie, H. Zhou, N. Campbell, P. J. Ryan, Y. Choi, J.-W. Kim, J. R. Patzner, S. Ryu, J. P. Podkaminer, J. Irwin, Y. Ma, C. J. Fennie, M. S. Rzchowski, X. Q. Pan, V. Gopalan, J. M. Rondinelli, C. B. Eom, *Nature* **2016**, *533*, 68.

[18] R. I. Eglitis, *Int. J. Mod. Phys. B* **2014**, *28*, 1430009.

[19] S. Middey, P. Rivero, D. Meyers, M. Kareev, X. Liu, Y. Cao, J. W. Freeland, S. Barraza-Lopez, J. Chakhalian, *Sci. Rep.* **2015**, *4*, 6819.

[20] Y. Liang, W. Li, S. Zhang, C. Lin, C. Li, Y. Yao, Y. Li, H. Yang, J. Guo, *Sci. Rep.* **2015**, *5*, 10634.

[21] J. L. Blok, X. Wan, G. Koster, D. H. A. Blank, G. Rijnders, *Appl. Phys. Lett.* **2011**, *99*, 151917.

[22] Y. Kuroiwa, S. Aoyagi, A. Sawada, J. Harada, E. Nishibori, M. Takata, M. Sakata, *Phys. Rev. Lett.* **2001**, *87*, 217601.

[23] Y. L. Zhu, X. L. Ma, D. X. Li, H. B. Lu, Z. H. Chen, G. Z. Yang, *Acta Mater.* **2005**, *53*, 1277.

[24] S. M. Anthony, S. Granick, *Langmuir* **2009**, *25*, 8152.

[25] Y. L. Tang, Y. L. Zhu, Y. J. Wang, W. Y. Wang, Y. B. Xu, W. J. Ren, Z. D. Zhang, X. L. Ma, *Sci. Rep.* **2015**, *4*, 4115.

[26] C. L. Jia, S. B. Mi, K. Urban, I. Vrejoiu, M. Alexe, D. Hesse, *Phys. Rev. Lett.* **2009**, *102*, 117601.

[27] S. J. Pennycook, *Philos. Trans. R. Soc., A* **2009**, *367*, 3709.

[28] Y.-M. Kim, A. Morozovska, E. Eliseev, M. P. Oxley, R. Mishra, S. M. Selbach, T. Grande, S. T. Pantelides, S. V. Kalinin, A. Y. Borisevich, *Nat. Mater.* **2014**, *13*, 1019.

[29] C. T. Nelson, B. Winchester, Y. Zhang, S.-J. Kim, A. Melville, C. Adamo, C. M. Folkman, S.-H. Baek, C.-B. Eom, D. G. Schlom, L.-Q. Chen, X. Pan, *Nano Lett.* **2011**, *11*, 828.

[30] C. L. Jia, S.-B. Mi, K. Urban, I. Vrejoiu, M. Alexe, D. Hesse, *Nat. Mater.* **2008**, *7*, 57.

[31] Y. Liu, Y.-J. Wang, Y.-L. Zhu, C.-H. Lei, Y.-L. Tang, S. Li, S.-R. Zhang, J. Li, X.-L. Ma, *Nano Lett.* **2017**, *17*, 7258.

[32] S. R. Zhang, Y. L. Zhu, Y. L. Tang, Y. Liu, S. Li, M. J. Han, J. Y. Ma, B. Wu, Z. H. Chen, S. Saremi, X. L. Ma, *Adv. Mater.* **2017**, *29*, 1703543.

[33] H. N. Lee, S. M. Nakhmanson, M. F. Chisholm, H. M. Christen, K. M. Rabe, D. Vanderbilt, *Phys. Rev. Lett.* **2007**, *98*, 217602.

[34] C.-L. Jia, V. Nagarajan, J.-Q. He, L. Houben, T. Zhao, R. Ramesh, K. Urban, R. Waser, *Nat. Mater.* **2007**, *6*, 64.

[35] M. Ahart, M. Somayazulu, R. E. Cohen, P. Ganesh, P. Dera, H.-k. Mao, R. J. Hemley, Y. Ren, P. Liermann, Z. Wu, *Nature* **2008**, *451*, 545.

[36] P.-E. Janolin, P. Bouvier, J. Kreisel, P. A. Thomas, I. A. Kornev, L. Bellaiche, W. Crichton, M. Hanfland, B. Dkhil, *Phys. Rev. Lett.* **2008**, *101*, 237601.

[37] Y. Liu, Y.-L. Zhu, Y.-L. Tang, Y.-J. Wang, Y.-X. Jiang, Y.-B. Xu, B. Zhang, X. L. Ma, *Nano Lett.* **2017**, *17*, 3619.

[38] Y. L. Tang, Y. L. Zhu, X. L. Ma, *Ultramicroscopy* **2016**, *160*, 57.

[39] Y. L. Tang, Y. L. Zhu, Y. Liu, Y. J. Wang, X. L. Ma, *Nat. Commun.* **2017**, *8*, 15994.

[40] I. Vrejoiu, G. L. Rhun, L. Pintilie, D. Hesse, M. Alexe, U. Gösele, *Adv. Mater.* **2006**, *18*, 1657.

[41] M. F. Chisholm, W. Luo, M. P. Oxley, S. T. Pantelides, H. N. Lee, *Phys. Rev. Lett.* **2010**, *105*, 197602.

[42] W. Zhong, R. D. King-Smith, D. Vanderbilt, *Phys. Rev. Lett.* **1994**, *72*, 3618.

[43] D. D. Fong, C. Cionca, Y. Yacoby, G. B. Stephenson, J. A. Eastman, P. H. Fuoss, S. K. Streiffer, C. Thompson, R. Clarke, R. Pindak, E. A. Stern, *Phys. Rev. B* **2005**, *71*, 144112.

[44] S. C. Abrahams, S. K. Kurtz, P. B. Jamieson, *Phys. Rev.* **1968**, *172*, 551.

[45] A. M. Glazer, S. A. Mabud, *Acta Crystallogr., Sect. B: Struct. Crystallogr. Cryst. Chem.* **1978**, *34*, 1065.

[46] C. W. Huang, W. Ren, V. C. Nguyen, Z. Chen, J. Wang, T. Sritharan, L. Chen, *Adv. Mater.* **2012**, *24*, 4170.

[47] H.-M. Zhang, M. An, X.-Y. Yao, S. Dong, *Front. Phys.* **2015**, *100*, 107701.

[48] I. Ponomareva, L. Bellaiche, *Phys. Rev. B* **2006**, *74*, 064102.

[49] R. E. Cohen, *Nature* **1992**, *358*, 136.

[50] J. Chen, K. Nittala, J. S. Forrester, J. L. Jones, J. Deng, R. Yu, X. Xing, *J. Am. Chem. Soc.* **2011**, *133*, 11114.

[51] C. Cazorla, M. Stengel, *Phys. Rev. B* **2015**, *92*, 214108.

[52] Z. A. D. Lethbridge, R. I. Walton, A. S. H. Marmier, C. W. Smith, K. E. Evans, *Acta Mater.* **2010**, *58*, 6444.

[53] R. H. Baughman, J. M. Shacklette, A. A. Zakhidov, S. Stafström, *Nature* **1998**, *392*, 362.

[54] Z. Gao, X. Dong, N. Li, J. Ren, *Nano Lett.* **2017**, *17*, 772.

[55] D. T. Ho, S.-D. Park, S.-Y. Kwon, K. Park, S. Y. Kim, *Nat. Commun.* **2014**, *5*, 3255.

[56] L. Fan, J. Chen, Y. Ren, Z. Pan, L. Zhang, X. Xing, *Phys. Rev. Lett.* **2016**, *116*, 027601.

[57] H. Liu, J. Chen, L. Fan, Y. Ren, Z. Pan, K. V. Lalitha, J. Rödel, X. Xing, *Phys. Rev. Lett.* **2017**, *119*, 017601.

[58] H. Fu, R. E. Cohen, *Nature* **2000**, *403*, 281.

[59] D. Damjanovic, *Appl. Phys. Lett.* **2010**, *97*, 062906.

[60] B. Noheda, D. E. Cox, G. Shirane, J. A. Gonzalo, L. E. Cross, S.-E. Park, *Appl. Phys. Lett.* **1999**, *74*, 2059.

[61] R. Guo, L. E. Cross, S-E. Park, B. Noheda, D. E. Cox, G. Shirane, *Phys. Rev. Lett.* **2000**, *84*, 5423.

[62] W. Ma, *AIP Adv.* **2016**, *6*, 045310.